

Analysis of the particle interactions in a two-dimensional-plasma dust crystal and the use of dust as a probe of the time-averaged presheath electric field

G. A. Hebner, M. E. Riley, and K. E. Greenberg*

Sandia National Laboratories, Albuquerque, New Mexico 87185

(Received 5 April 2002; published 14 October 2002)

A method for measuring the interactions of dust particles within a two-dimensional (2D) layer in a plasma is presented, along with the use of dust as a probe for determining plasma presheath electric fields. Particle interactions were directly determined from the lateral compression of two-dimensional plasma dust crystals confined in a parabolic potential well. The shape of the parabolic potential well was confirmed by observing trajectories of single particles falling within the well. Particle trajectories were in good agreement with values calculated using gas temperatures derived from laser-induced-fluorescence measurements of the argon metastable velocity distributions and assuming diffusive gas scattering. Measured particle separations combined with an equation of state for the crystal were used to derive values for the plasma screening length and the charge on the particles. Screening lengths and charges were measured for a range of plasma power, pressure, and particle diameter (mass). Analysis of the particle heights and charge were used to derive the time-averaged electric fields at the edge of the rf driven plasma sheath. Measured electric fields were between 5 and 22 V/cm. For smaller particle diameters, the ion wind force was comparable to the force of gravity. These measurements showed that the particles are confined to the bulk-plasma side of the classical Bohm point.

DOI: 10.1103/PhysRevE.66.046407

PACS number(s): 52.27.Lw, 52.40.Kh, 52.70.Nc, 51.20.+d

I. INTRODUCTION

The plasma presheath region, the transition region between the bulk plasma and the classical sheath near surfaces imbedded in the plasma, has received little experimental or theoretical attention. The plasma presheath is an interesting part of the discharge because in this region the plasma begins to change from a quasineutral charge balance to a space-charge-dominated plasma as the ion and electron densities begin to differ. Traditionally, one side of the presheath is defined by the Bohm point, the point in the sheath where the ion energy is equal to the electron temperature in energy units. The other side of the presheath, the point in the bulk plasma where the electric field begins to deviate from the value in the bulk plasma, has no practical definition.

Experimentally and theoretically, the plasma presheath region is challenging. For example, it is difficult to directly measure the presheath electric fields since most diagnostic probes introduce unacceptable perturbations due to their own undefined sheaths. While optical experiments have measured the shape of the electric field in the sheath for both direct current and radio frequency (rf) driven discharges, the electric fields present in the presheath region are too small for most diagnostic techniques [1–3]. Recently, Oksuz and co-workers used a Mach probe and laser-induced fluorescence to measure the ion velocity in the presheath region of a dc discharge [4]. They showed a distinct transition from linear to nonlinear scaling of ion velocity. Theoretically, the presheath region is also challenging since subtle changes in the field, slight departures from perfect velocity distributions, and difficulties in boundary conditions can have an impact

on the accuracy. Riemann has developed a model of the presheath plasma potential in which $\Phi \propto \sqrt{x}$, where x is the spatial location [5].

In this work, we show how characteristics of plasma dust crystals can be used to ascertain the electric field distribution in the presheath region of an rf discharge. In order to use dust crystal properties to determine the presheath field, it is necessary to accurately measure the charge that accumulates on the dust particles. We have developed a systematic procedure for determining the charge on the dust particles by analyzing the crystalline structure. Using this systematic approach to find the accumulated charge on particles of various masses, we have been able to determine the presheath field distributions and to test Riemann's model of the presheath.

Plasmas containing dust particles occur in fields as diverse as interstellar space and microelectronics processing discharges. Under appropriate conditions, first identified in 1994 [6,7], the dust particles will assemble into a crystalline structure. Since those first observations, experiments and analyses have examined interaction mechanisms and collective properties [8,9]. In a more general view, plasma dust crystals are a subset of broader work to understand the structure and dynamics of charged particle assemblies [10–14]. Examples of such systems range from laser cooled ions confined by traps [15,16] to colloids trapped between glass plates [17,18]. It has been established that shorter-range shielded Coulomb interactions typical of our system form close-packed arrays rather than the Wigner ring structure of two-dimensional (2D) Coulomb interactions [11,13].

Most plasma dust experiments are performed using micron-sized particles in rf-excited, parallel-plate discharges. In the plasma, injected dust particles charge negatively as they drift downward under the influence of gravity. The dust forms a levitated layer of particles above the lower electrode at the point where the vertical electrostatic forces produced

*Present address: Career Enrichment Center, Albuquerque Public Schools, 807 Mountain Rd. NE, Albuquerque, NM 87102.

by the electrode plasma sheath are counterbalanced by gravity. Weak radial components of the forces then can cause the dust particles to form an ordered, 2D structure characterized by a dominant hexagonal closed-packed structure, a plasma dust crystal. An accurate measurement of the charge on the particles at this point in the plasma can be used to derive the sheath electric field.

In most experiments, the horizontal confining forces on the 2D plasma dust crystal are many orders of magnitude weaker than the vertical confining forces. Thus, knowledge of the radial or horizontal confining forces is critical in determining the properties of the resulting 2D crystal. In the majority of the experiments to date, a confinement ring or structure placed on the flat lower electrode provides the radial confinement. However, since the plasma sheath cannot exactly conform to the shape of the structure due to a finite Debye shielding length, the shape and uniformity of the resulting potential well and the magnitude of the radial confining forces are spatially nonuniform and difficult to quantify. We report in detail the use of a curved lower electrode with a spherical radius of curvature R_c to provide a well-characterized transverse confining force (pressure) on the 2D plasma crystals [19]. We analyze the compression of the 2D layer subjected to this pressure to determine the constitutive interaction of the particles, which is a repulsive Debye-shielded Coulomb field with dust charge $-Ze$ and shielding length λ . Z and λ are required to characterize the interparticle potentials, to examine details of the particle sheath and charging, and to evaluate the influence of ion wake fields on multilayer plasma crystal formation [20]. For our experimental conditions, the plasma sheath conformed to the spherical depression in the lower electrode since the Debye length and the sheath thickness were much smaller than R_c .

In prior work, λ has been determined from Langmuir probe measurements of plasma properties [21,22] or laser excitation of horizontal waves in the dust crystal [23]. Measurements of Z have relied on laser and rf excited resonance techniques [24], and models of the electrode sheath [25]. In contrast with prior work, our analysis does not rely on measurements of the plasma parameters and/or analytic models of the plasma sheath. Finally, parabolic lower electrodes [26] or traps formed by glass cylinders [27,28] have previously been used to provide particle confinement. However, that work did not examine larger crystals or analyze the response of the crystal to external forces, which is the focus of this work.

II. EXPERIMENTAL CONFIGURATION

The experiments were performed in an asymmetrically driven, parallel-plate discharge chamber, a modified gaseous electronics conference (GEC) rf reference cell [29] shown in Fig. 1. A 6-mm-thick, 100-mm-diameter aluminum disk with 50-mm-diameter interchangeable inserts of various radii of curvature was placed on the standard GEC capacitively coupled rf-driven lower electrode. The electrode was driven at 20 MHz using a signal generator, power amplifier, and L matching network. Power into the plasma was measured using an in-line power meter and the voltage and current were

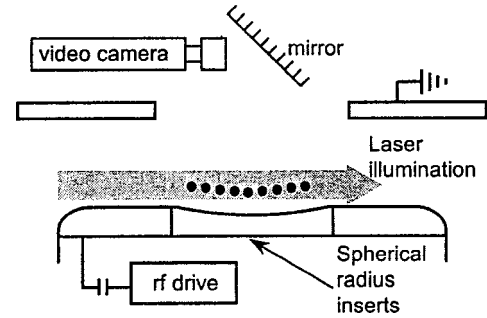


FIG. 1. Experimental setup. The grounded upper electrode was a ring with an outer diameter of 165 mm, inner diameter of 76 mm, and an interelectrode spacing of 30 mm. A 6-mm-thick, 100-mm-diameter aluminum disk with 50-mm diameter interchangeable inserts of various radii of curvature was placed on the rf driven lower electrode.

measured using previously reported voltage and current measurement techniques and probes [29]. The grounded upper electrode was a 4-mm-thick ring with a 165-mm outer diameter and a 76-mm inner diameter. Interelectrode spacing was 30 mm. Argon gas flow was 1–4 SCCM (cubic centimeters per minute at STP). To eliminate the influence of gas motion on the crystal shape, the gas was injected into and pumped out of the lower, baffled chamber of the GEC reference cell. For some gas injection configurations, gas motion strongly influenced the stability of the plasma crystal or induced rotations.

Melamine particles with diameters between 4.5 and 11.9 μm were dropped into the plasma through the opening in the upper electrode. Particles were injected by mechanically tapping a particle-containing “salt shaker” constructed from an aluminum cup with a hole on the bottom that was covered with 500 line/inch mesh. The crystal was illuminated using a 0.2-mm-thick sheet of light produced by a 532 nm, 10 mW laser, scanning mirror, and cylindrical lens. The particles rapidly fell from the top down to the region just above the lower electrode, where they slid laterally towards the center of the electrode. In all cases, the plasma crystals were confirmed single layer by observing the crystals from the side. The crystals were stable over long periods of time (hours).

Power into the plasma, voltage on the driven electrode, and the dc bias voltage are shown in Fig. 2 as functions of the signal generator voltage and pressure. Typical rf powers into the plasma were 1.8–6 W, V_{p-p} of 40–110 V, and dc self-bias of -10 to -60 V. Electron density varied between 3×10^8 and $8 \times 10^8 \text{ cm}^{-3}$ while electron temperature was 2.6–3.6 eV, as determined by a Langmuir double probe.

An example of a single-layer plasma crystal containing 434 particles with a diameter of $8.34 \pm 0.09 \mu\text{m}$ is shown in Fig. 3. A change in nearest-neighbor (NN) spacing s_{NN} with radial position is readily observable. The radial compression, as discussed below, is due to the collective weight of the outer particles acting on the inner particles. In addition, all of our crystals showed a planar hexagonal-close-packed (hcp) crystal structure [11,13]. Due to the cylindrically symmetric potential well, there were always a few packing defects within the hcp arrangement. Images similar to Fig. 3 were

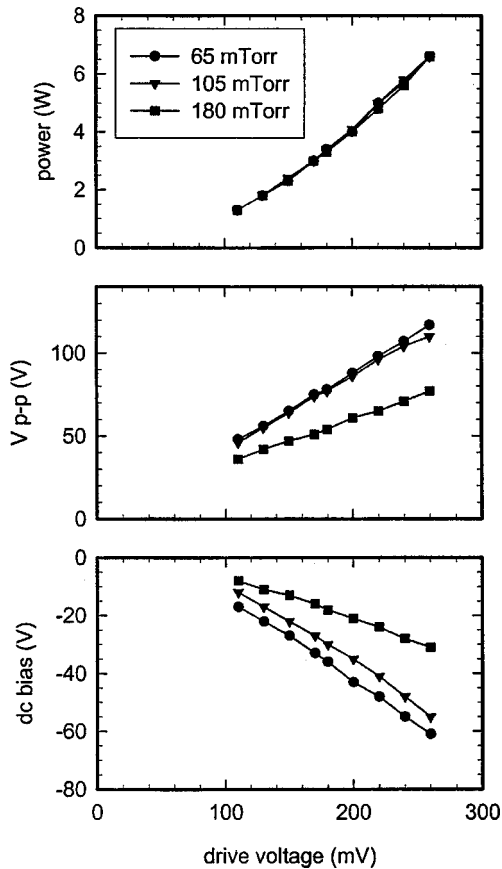


FIG. 2. Power into the plasma, peak-to-peak voltage on the driven electrode and the dc bias voltage as functions of the signal generator drive voltage and argon pressure.

analyzed for the total number of particles N_{tot} , the radius of the crystal r_{max} , and the NN spacing in the center of the crystal s_0 . Our experimentally observed radially dependent s_{NN} is in good qualitative agreement with prior calculations for isolated single charge systems [11] and plasma crystal systems [14].

Custom image processing algorithms were used to identify the particle locations in single frame images obtained using a standard digital camera or a time series of images obtained from digitizing video tape. For example, in the plasma crystal compression experiments, images of the plasma crystals were obtained using a high-resolution digital camera. Particle locations were extracted and analyzed for interparticle spacing and crystalline structure parameters. Time-dependent trajectories of the injected particles were captured on video tape using a coupled-channel device (CCD) camera and lens. The video tape was then digitized frame by frame and the particle position was extracted using our algorithms. Our image processing algorithms generally follow the procedure outlined by Crocker and Grier for colloidal particle systems [30], with modifications due to our relatively sparse particle spacing.

III. THEORETICAL DEVELOPMENT

While molecular dynamics (MD) simulations can potentially reproduce the experimentally observed features of

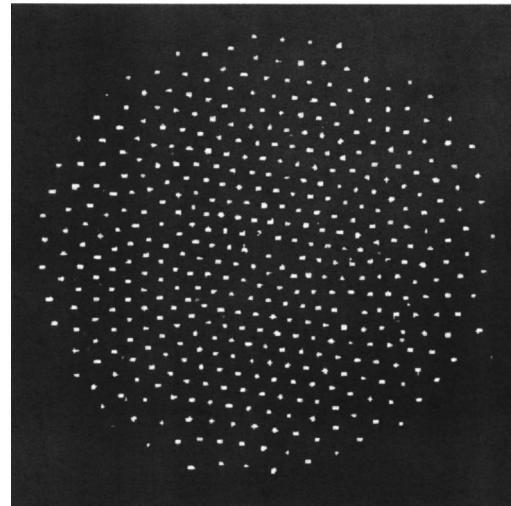


FIG. 3. An example of a 14-mm-diameter, single-layer plasma crystal containing 434 particles formed above the parabolic well in the lower electrode. Power into the plasma was 1.8 W, pressure was 110 mTorr and $R_c = 0.5$ m. Note the change in a nearest-neighbor spacing with radial position. The smaller spots are optical reflections off the lower electrode.

plasma crystals [11,12,14], an equation-of-state (EOS) treatment avoids a statistical analysis of *both* experimental and theoretical MD simulations to extract the particle interaction parameters. In order to establish a relation among the macroscopic EOS observables such as radius and density of the 2D plasma crystal, we must have a constitutive relation involving the particle interactions. The confinement of the particles can be pictured as the settling of particles into the bottom of a geometric “bowl,” which is approximately parabolic. Irrespective of whether the downward force is dominated by gravity or by ion wind effects, the important point is that the shape of the potential well can be determined from observations of the dynamics of a single particle as it falls into the potential well. The shape of the potential well determines the radial component of the force applied to the layer of particles. From this radial force and the density variation within the particle layer, information about the pairwise interaction of the individual particles can be determined.

We also assume that the presence of many particles does not change the basic properties of the plasma in the vicinity of the sheath. Measurements of the spatially resolved optical emission tend to support this assumption. Total optical emission was measured using a gated, intensified CCD camera for a range of crystal diameters from 0 to 3 cm. Those measurements showed a less than $\pm 2\%$ change in the optical emission when particles were added to the plasma.

An important point is that a truly perfect crystal arrangement may not exist when confined in a spatially varying force field. The particles will arrange into an ordering that is only locally perfect. In other words, the crystals contain defects. However this amount of crystallinity is sufficient to allow us to characterize the internal energy, pressure, and density of the layer of dust particles at a particular location. The state properties of the dust layer can be related to the

pair interactions of the particles, which is the focus of our work.

A. Equations of motion of plasma dust particles

In the present experimental arrangement with cylindrical symmetry about the vertical axis defined by gravity, the plasma dust particles are suspended in a nearly planar region at the bottom of the plasma, at the edge of the plasma sheath. Consider a system with the z axis pointed upwards. Newton's equation for a single dust particle with position $\vec{r}(t)$ is

$$m_d \ddot{\vec{r}} = -\hat{e}_z m_d g + q_d \vec{E}_{\text{sh}} - m_d \gamma_{\text{gas}} \dot{\vec{r}} + \vec{f}_w + \vec{f}_{\text{tp}}, \quad (1)$$

where we use overdot notation to denote time derivatives. z is the dust particle vertical coordinate, m_d is the mass of the dust particle, g is the acceleration of gravity, q_d is the charge on the particle, \vec{E}_{sh} is the plasma sheath electric field at the position of the particle, γ_{gas} is the damping coefficient due to collisions with the neutral gas background, \vec{f}_w is the “wind force” on the particle due to ion flow within the nonuniform plasma sheath, and \vec{f}_{tp} is the thermophoretic force due to temperature asymmetries in the background gas. The wind force includes all electrical forces on the particle due to its presence in a nonuniform plasma except for those forces isolated in the $q_d \vec{E}_{\text{sh}}$ term. We will use SI units unless otherwise noted. g and γ_{gas} are positive constants. The quantities q_d , f_w , f_{tp} , and \vec{E}_{sh} all can be functions of both \vec{r} and the particle velocity $\dot{\vec{r}}$.

1. Forces on particle due to neutral gas background

The damping coefficient γ_{gas} is derived by a gas-kinetic analysis, allowing for the small size of the dust particles and the large mean free path of the gas atoms. The result for the force acting on a spherical dust particle due to specular reflection of the gas species with mass m_{gas} number density n_{gas} , and temperature T_{gas} is [31]

$$\vec{f}_{\text{gas}} \approx -\frac{4}{3} \pi a^2 m_{\text{gas}} n_{\text{gas}} \nu_{T_{\text{gas}}} \vec{v}_d, \quad (2)$$

where $\vec{v}_d = \dot{\vec{r}}$ is the particle velocity relative to the stationary gas and $\nu_{T_{\text{gas}}} = (8kT_{\text{gas}}/\pi m_{\text{gas}})^{1/2}$ is the thermal velocity (mean speed) of the gas atoms. The particle radius is denoted as a . The damping coefficient is

$$\gamma_{\text{gas}} = \frac{4}{3} \pi a^2 m_{\text{gas}} n_{\text{gas}} \nu_{T_{\text{gas}}} / m_d. \quad (3)$$

Equation (3) may be rewritten as

$$\gamma_{\text{gas}} = \sqrt{\frac{8m_{\text{gas}}}{\pi k T_{\text{gas}}}} \frac{P_{\text{gas}}}{a \rho_d}, \quad (4)$$

where P_{gas} is the gas pressure and ρ_d is the density of the particle. There is some uncertainty in the proper value to use for the damping coefficient because of the unknown elastic and inelastic scattering properties of the gas on the particle surface. We note that the case of complete sticking of the gas on the particle surface would give the identical coefficient as given in Eq. (4) [31]. Diffuse elastic scattering would in-

crease γ_{gas} by a factor of $1 + \pi/8 = 1.3927$ [31], which we believe to be the realistic value. Complete thermal accommodation of a gas atom on a dust particle at a different temperature T_{surf} would increase the drag by a factor [32] of $1 + (\pi/8) \sqrt{T_{\text{surf}}/T_{\text{gas}}}$, a change that might be important considering the continual delivery of energy to the dust particles in their action as a catalyst for plasma recombination.

The imprecise knowledge of temperature gradients and non-Maxwellian properties of the gas complicate the thermophoretic force [33]. The mean free path is always much larger than the particle sizes in our system, but that path may be comparable to the dimensions of the physical boundary separations. The characterization of the thermophoretic forces is ameliorated here by the fact that we can design the system so that this force and the plasma electric force are not crucial to the analysis for determining Z and λ . For this experimental geometry, we will demonstrate that thermophoretic forces are likely not important.

2. Electric field within the plasma presheath

In order to calculate the electric field from first principles, we would need a reasonably accurate simulation for the sheath and presheath region. This simulation would have to be time dependent for most of the situations of interest. Instead, we will use a phenomenologically characterized time-averaged model for the plasma electric field that incorporates most of the important features leading to dust crystallization and dust particle dynamics. As described later, our phenomenological form is in good agreement with measurements.

The experimental situation is that of an azimuthally symmetric system. Cylindrical coordinates r and z will be used to describe the fields in this section. We assume that the plasma potential in the region of the electrode is dominantly a function of z with a small r -dependent shift in height. This is expressed by writing the electric potential as a function of only the vertical coordinate with an r -dependent shift, which is approximately quadratic in radius,

$$\begin{aligned} \phi &= \phi(z - h(r)), \\ h(r) &\approx cr^2. \end{aligned} \quad (5)$$

The replacement of h by a quadratic will be introduced later when needed. The constant c is related to the radius of curvature of the “confining bowl” by $c = \frac{1}{2} R_c$. The electric field resulting from the potential in Eq. (5) is found to be

$$\vec{E}_{\text{sh}}(r, z) = -[\hat{e}_z - \hat{e}_r h'(r)] \phi'(z - h(r)), \quad (6)$$

where the primes denote first derivative with respect to the argument. The choice of functional form of $\phi(z)$ will strongly affect the particle motion in the vertical z direction, including the location of the particle equilibrium position. The choice of $h(r)$ will affect the lateral motion of particles trapped in the potential minimum, which itself is created by the z dependence of all the forces.

We will use a phenomenologically characterized sheath potential for $\phi(z)$. The form for $\phi(z)$ is that of a quadratic in z connected smoothly to an exponential decaying towards

the plasma bulk. Experimentally, a quadratic form for $\phi(z)$ is a good approximation in the high field region of the sheath [1–3] but as we will show, an exponential is a better fit in the region where the plasma crystal layer levitates. The position of the joining point, the value of the potential at the electrode relative to the bulk, and the decay constant of the exponential are all independently adjustable and make it possible to fit the important features of whatever might be known about the sheath and presheath of the plasma.

3. The ion wind force

The ion wind force on the dust particle is due to the scattering of ions off the dust particle as they flow towards the electrode. We use the cross section that has been computed for the momentum transfer [34]. The ions and dust particles are moving in three dimensions and we must obtain the correct vector dependence of the wind force.

First of all we assume that the ion flow velocity, $\vec{v}_{\text{ion}} \equiv \vec{v}_{\text{wind}}$, is parallel to the electric field within the sheath. This is not a bad assumption, as the ions respond to the field much more rapidly than the particles. Whether the ion flow is collisional (fluid or drift diffusion) or the ions are in free fall, their motion is dominantly along the electric field vector. Thus the wind force on a stationary dust particle is directed along \vec{E}_{sh} and the force on a moving particle is obtained from the vector addition of the velocities. For example, a moving particle in a stationary ion background has a wind force that opposes the particle velocity. The wind force is given in terms of the momentum-transfer cross section $\sigma_{\text{ml}}(\nu_{\text{rel}})$, where ν_{rel} is the relative ion-particle velocity,

$$\vec{v}_{\text{rel}} = \vec{v}_{\text{ion}} - \vec{v}_d, \quad (7)$$

$$\vec{f}_w = n_{\text{ion}} \nu_{\text{rel}} m_{\text{ion}} \vec{v}_{\text{rel}} \sigma_{\text{ml}}(\nu_{\text{rel}}). \quad (8)$$

Because the ion velocity, drift or kinetic, is always much larger than the dust particle velocity, we can replace \vec{v}_{rel} by \vec{v}_{ion} in most of the analysis. In this case the product $n_{\text{ion}} \nu_{\text{ion}}$ in the wind force is just the ion flux Φ_{ion} flowing through the plasma sheath. This is immediately related to the ion current, or to the plasma density and the Bohm velocity.

4. Charging of particles due to electron and ion impact

We will use the orbital motion limited theory of Mott-Smith and Langmuir to calculate the time-dependent charging and discharging of the dust particles when doing full solutions of the time-dependent equations of motion of the dust movement [35]. This is identical to the most commonly used approximations for particle charging, except for our modifications to match to the local potential at the particle position. In calculating the charge from the rate of electron and ion impact, we will include any time lag in the relation of particle charge to the instantaneous position within the plasma sheath. We will assume that the collisions with the particle result in unit sticking or accommodation on the particle surface. This is not necessarily true, and corrections can easily be made if more information is known about the pro-

cess. The charging rate of a particle is written in terms of the incident ion and electron currents to the surface,

$$\dot{q}_d = I_i + I_e. \quad (9)$$

The electron current is evaluated in terms of the Boltzmann assumption about the electron distribution function in the sheath and plasma. We assume that the electrons are distributed at a temperature T_e throughout the plasma. The local density is related to the bulk (or Bohm point) density by means of the Boltzmann distribution in order to simplify the result,

$$\begin{aligned} I_e &= -e4\pi a^2 \Phi_{\text{ed}} \\ &= -e4\pi a^2 \frac{1}{4} n_e(\vec{r}) \nu_{\text{Te}} \exp[e(V_d - \phi(\vec{r}))/kT_e] \\ &= -e\pi a^2 n_B \nu_{\text{Te}} \exp[e(V_d - V_B)/kT_e], \end{aligned} \quad (10)$$

where Φ_{ed} is the electron flux on the surface, ν_{Te} is the electron thermal velocity, $\nu_{\text{Te}} = (8kT_e/\pi m_e)^{1/2}$, and the potential V_B at the Bohm reference point is defined to be zero. The only dynamic dependence remaining in I_e is in the surface potential. The rise in (negative) potential at the dust surface above the local sheath potential is estimated from the capacity relation of a charged sphere,

$$V_d - \phi(\vec{r}) \approx \frac{1}{4\pi\epsilon_0} q_d/a. \quad (11)$$

One could treat either V_d or q_d as the unknown property of the particle for the purposes of numerical solution.

The ion current is not so easily approximated due to the ion orbiting. We use the microcanonical distribution function for ions ignoring multiple turning points and absorptive corrections. This limiting case of the complex general theory gives

$$\begin{aligned} I_i &= e\pi a^2 n_i(\vec{r}) \nu_i(\vec{r}) \left(1 - \frac{e\Delta V}{K_i(\vec{r})}\right) \\ &= e\pi a^2 \Phi_i \left(1 - \frac{e(V_d - \phi(\vec{r}))}{K_i(\vec{r})}\right), \end{aligned} \quad (12)$$

where ΔV is the fall in the potential of an ion as it encounters the particle surface at the local position in the sheath. The ion flux Φ_i is constant through the sheath. $K_i(\vec{r})$ is the kinetic energy of the ions at position \vec{r} within the sheath, which can be approximated from the fall through the sheath potential. If we sum the electron and ion currents to zero, we obtain a value for the steady state, equilibrium charge, and potential carried by the particle. Equations (10) and (12), due to Mott-Smith and Langmuir, are called the orbital motion limited theory of charging [35], except for our modifications to match to the local potential at the particle position.

Our formulation includes all time-dependent effects due to motion of the particles within a time-averaged sheath field, but does not include the time dependence of the rf field or plasma itself. It is known that the rf field can affect the charging of the dust particles [36]. The major effect here of course is the electron density, which has a strong rf compo-

ment. The ions, and certainly the particles, do not respond significantly to the rf field. An rf variation in electron density could produce substantial changes in the dust charge as our charging frequency is nearly the order of the rf. A consequence of this is the fact that the charging rate of the dust forces an extremely stiff numerical problem in the coupled solution to the dust motion equations. However, all of our experiments have the dust trapped on the plasma side of the Bohm point as defined by our time-independent formulation. The rf effects on plasma charge separation, i.e., electron density, are small there, and the cycle-averaged rf charging rates of the dust particles should be nearly those of a dc sheath because the electron charging rate is linear in the local electron density. However, there is no question that dust particles trapped in the more charged region of a strongly driven rf sheath would require a full time-dependent treatment of the sheath, requiring a revision of the formulation of Sec. III A 2.

Thus all the dynamical forces acting on a dust particle are now known in terms of the plasma properties. These can be used in the Newtonian equation of motion for the particle to observe its trajectory when dropped into the plasma. If we add particle-particle interactions, we are ready to do multi-particle dynamics. However, for the purposes at hand, we will not be looking at particle dynamics except in the equilibrium layer formed with several particles. Nevertheless we will need to have the function $h(r)$ or the quadratic coefficient c characterizing the curvature of the potential field.

B. Equation of state for a 2D confined disklike particle layer

Consider a particle to be at equilibrium in the curvilinear coordinate measured along the local plasma electric field direction $\hat{E}(r, z)$, which is very close to the vertical direction. This requires that this component of the force is zero. Because the wind force vector closely parallels the electric field vector, we know that only gravity and the viscous forces can act to accelerate or decelerate the particle in the lateral direction perpendicular to $\hat{E}(r, z)$. It is sufficient just to consider the forces of gravity and electric field acting in the vertical direction. We will neglect the thermophoretic force as mentioned previously. This allows us to write the r component of the force from Eq. (1) in a simplified form because of the equilibrium in the vertical coordinate,

$$\begin{aligned} f_z &= -m_d g - q_d \phi'(z - h(r)) = 0, \\ f_r &= h'(r) q_d \phi'(z - h(r)) = -h'(r) m_d g, \\ f_r &\approx -2c r m_d g \equiv -k r. \end{aligned} \quad (13)$$

The first relation in Eq. (13) expresses the condition for equilibrium (force balance) in the vertical coordinate. The second relation uses the vertical force balance to simplify the radial component of the force. This radial component is independent of z because of the functional form of the approximation for the electric potential in Eq. (5). The constant $k = 2m_d g c = m_d g / R_c$ is a harmonic restoring force constant for the lateral motion about the center of the potential well if it is parabolic.

Experimentally, the particles are found to be arranged in a monolayer, hcp lattice for the most part. The crystal is not perfect however, as the compression forces the density to be larger at the center than at the perimeter of the disk. Thus there are several defects within the lattice. Knowing this, we can simplify the above analysis of the balance between the repulsive pair interaction potential and the applied compressive force. The theory that we derive in this section is a continuum mechanics limit of the discrete particle layer. Let $s(r)$ denote the NN spacing in the hcp lattice, where the radius is written to acknowledge that the average spacing will vary within the disklike layer. The areal number density is related to the hcp NN spacing by

$$n = 2/\sqrt{3}s^2 = 1.1547/s^2, \quad (14)$$

on the average at any point within the crystal.

We will take the pairwise interaction potential energy between the particles to be a function of the separation s of the particles, $V_{\text{pair}}(s)$. Thus, although the argument of V_{pair} might naturally be the spherical coordinate, in fact it is really only the cylindrical coordinate appropriate for the 2D layer of dust particles. The potential energy per particle within a hcp lattice is $3V_{\text{pair}}(s)$ when NN interactions dominate. We will discuss corrections to the NN assumption below. The potential energy density within the layer is given by

$$e(r) = 3n(r)V_{\text{pair}}(s(r)), \quad (15)$$

which is in units of energy per area in a 2D geometry.

From the steady-state Euler equation giving the momentum relation for a continuum fluid, or just from simple addition of forces, one can argue that the radial equation relating the pressure $p(r)$ and external force applied to the layer is

$$\begin{aligned} dp(r)/dr &= F_r(r) = n(r)f_r(r) = -n(r)m_d g h'(r) \\ &\approx -k r n(r), \end{aligned} \quad (16)$$

where F_r is the force per area within the layer and f_r is the force on an individual particle as given in Eq. (13). The parabolic approximation enables several simple relations to be derived, relating pressure to particle density variation; but that will not be pursued until later.

Pressure is defined by the change in energy with volume $dE = -p dA$, or with area in this two-dimensional case. Let the area be A , with N particles within A . The number density is $n = N/A$. Solving for p using Eq. (15) and the definitions of A and n gives

$$p = -\frac{dE}{dA} = -\frac{d[Ae(s)]}{d[N/n(s)]} = -\frac{d[3NV_{\text{pair}}(s)]}{Nd(\sqrt{3}s^2/2)} - \sqrt{3} \frac{dV_{\text{pair}}(s)}{s ds}. \quad (17)$$

This relation applies at any radius r within the layer where the local pressure is $p(r)$ and the NN separation is $s(r)$. However, it can only apply at the outer radius of the disk if the NN separation s is allowed to become infinite just beyond $r = r_M$, where r_M is the radius of the last ring of particles in the dust layer. This is consistent with zero density

for $r > r_M$. As $r \rightarrow r_M$ from smaller values, both $s(r)$ and $n(r)$ approach nonzero values. The appropriate boundary condition for the *outer set of particles* at the perimeter of the dust layer can be found by balancing the inward force due to the external field with the vector sum of the pairwise forces with the next inward group of particles. This leads to an approximate relation depending on the particle arrangement in the outer layer. The force balance relation is

$$\sqrt{3}V'_{\text{pair}}(s_M) = f_r(r_M) \approx -kr_M, \quad (18)$$

which is assuming an ideal crystal structure at the perimeter. In the limit of a minimum configuration of seven hcp particles, the $\sqrt{3}$ factor in this equation would become a factor of 2.

We can now combine Eqs. (16) and (17) to give a balance equation for the pressure within the layer,

$$\frac{dp(r)}{dr} = -\sqrt{3} \frac{d}{dr} \frac{dV_{\text{pair}}(s)}{s ds} = n(r)f_r(r), \quad (19)$$

in which s is implicitly a function of r . The first integral can be found using the relation of n to s written in Eq. (14) and the expression for the radial component of the force given in Eq. (13),

$$\begin{aligned} \left[s \frac{dV_{\text{pair}}(s)}{ds} - 2V_{\text{pair}}(s) \right]_{s_0}^s &= -\frac{2}{3} \int_0^r dr' f_r(r') \\ &= \frac{2}{3} m_d g [h(r) - h(0)], \quad (20) \\ &\approx \frac{2}{3} m_d g c r^2 \equiv \frac{1}{3} k r^2, \end{aligned}$$

where the superscript and subscript on the square brackets indicate that the expression contained within is to be evaluated as $[f(x)]_a^b = f(b) - f(a)$. Boundary conditions have been applied such that $r=0$ corresponds to NN separation $s=s_0$ at the center of the layer. As $s \rightarrow s_M$, where s_M is the maximum pairwise separation within the layer, r approaches the radius of the disk, r_M . This expression for r_M is a function of s_0 , reflecting the fact that the compression of the layer at the center depends on the size and cumulative weight of the layer. This can only be determined by an integration of the differential relation connecting r and s .

The differential equation determining the variation of properties within the layer is found from Eq. (20) by reverting to the differential form for the Euler momentum equation,

$$\frac{ds}{dr} = \frac{2}{3} m_d g \frac{h'(r)}{s V''_{\text{pair}}(s) - V'_{\text{pair}}(s)}. \quad (21)$$

This is a highly nonlinear ordinary differential equation with a movable singularity for typical choices of the pair interaction. The boundary condition at zero radius will determine where the singularity occurs, which is somewhat beyond the location of the boundary of the particle layer r_M . Unfortunately, the necessity of doing a numerical solution for $s(r)$ is the price one pays for having an unspecified pair potential as well as a general form for the confining potential.

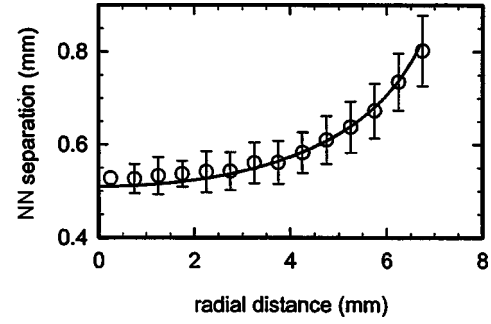


FIG. 4. Nearest-neighbor separations as functions of radial position for a plasma crystal containing 434 particles. The particle separations were grouped and averaged into 0.5 mm wide bins. The solid line was calculated using Eq. (21) with $s_0=0.51$ mm, $\lambda = 260 \mu\text{m}$, and $Z=23\,500$ electrons.

The radial compression of the plasma crystal can be used to further test the equation of state [Eq. (21)]. Experimentally measured NN spacing as a function of radial position for a plasma crystal containing 434 particles is shown in Fig. 4. The experimental data represents the average of all NN separations within a given radial bin, from the center of the nearly circular dust layer to the perimeter. For fixed N_{tot} , $s_{\text{NN}}(r)$ increases with r since the radial force balancing the interparticle repulsion is decreasing. The calculated NN separation using Eq. (21) is shown as the solid line in Fig. 4. Equation (21) was started with $s_0=0.51$ mm, and the Debye screening length and charge were fixed at $260 \mu\text{m}$ and $-23500e$. The Debye parameters were determined from additional analysis of the experimental data in a plasma of the identical properties, to be discussed below. The termination of the $s(r)$ curve was fixed by boundary conditions to be given shortly. In general, the equation of state provides excellent agreement with the absolute value of the NN separation and the shape of the experimental data for crystals with 30–1500 particles, indicating that the interparticle potential is well represented by a screened interaction. A recent study of particle-particle interactions [8] depended on the gas friction being small enough to carry out dynamic scattering experiments. Our method is not limited to such low gas pressures, but we cannot observe particle deflections. Thus our technique is complementary to previous work [8], and provides additional information about the interaction at an extended range [19].

1. Special forms of the equation of state for a parabolic confining well

If the r -dependent shift of the plasma field is quadratic [Eq. (5)], we can write some especially simple formulas for the relation of the pair interaction to the total number of particles trapped in a monolayer disk. In Eq. (19), we introduce $f_r = -kr$ on the right side and integrate from $r=0$ to r . This gives

$$p(r) - p(0) = -\frac{k}{2\pi} N_{<}(r), \quad (22)$$

where $N_{<}(r)$ is the number of particles within radius r . Allowing the radius to become larger than the radius of the disk reveals that

$$p(0) = -\sqrt{3} \frac{dV_{\text{pair}}(s)}{sd} \Big|_{s=s_0} = \frac{k}{2\pi} N_{\text{total}}, \quad (23)$$

where we have used the result for pressure given in Eq. (17) and defined N_{total} as the total number of particles in the disk. Again s_0 is the NN spacing at the center of the disk.

2. Special form of the pair interaction

The goal of this work is to derive interaction parameters from observations of the plasma crystal compression. We do that by choosing the NN pair interaction to be a Debye-shielded Coulomb potential,

$$V_{\text{pair}}^{\text{Debye}}(r) = \frac{(q_d^2/4\pi\epsilon_0)}{r} \exp(-r/\lambda), \quad (24)$$

where q_d is the total charge on the particle ($-Ze$) and λ is the screening length, the two parameters of interest. We note that no assumptions are made as to λ being the bulk plasma screening length. Evaluation of Eq. (20) with a parabolic form for $h(r)$ gives

$$r^2(s) = \frac{3}{k} \left[\left(3 + \frac{s}{\lambda} \right) V_{\text{pair}}^{\text{Debye}}(s) \right]_s^{s_0}, \quad (25)$$

using the same notation for the brackets as in Eq. (20). If we label the point in radius where the NN separation becomes infinite as r_∞ , we see that r_∞ is given by

$$r_\infty^2 = \frac{3}{k} \left(3 + \frac{s_0}{\lambda} \right) V_{\text{pair}}^{\text{Debye}}(s_0). \quad (26)$$

The singular point r_∞ , where $s \rightarrow \infty$, occurs at a point in radius greater than r_M . An approximate connection of r_∞ and r_M can be found to be

$$r_\infty \approx r_M + s_M \sqrt{3/2}. \quad (27)$$

This would enable a least-squares fit of the observed maximum radius as a function of s_0 in terms of the number of charges on the particle Z and the screening length λ .

We can also infer properties of V_{pair} as to the dependences on Z and λ from experimental observations of the radial variation of $s(r)$. However, it is more convenient from a regression aspect to use observations of $s_0 = s(0)$ as it varies with r_M or the total number of particles in the layer N_{total} . For this special form of the pair interaction, Eq. (23) becomes

$$\sqrt{3} \frac{1}{s_0} \left(\frac{1}{s_0} + \frac{1}{\lambda} \right) V_{\text{pair}}^{\text{Debye}}(s_0) = \frac{k}{2\pi} N_{\text{total}}, \quad (28)$$

which enables a least squares regression analysis of available data for NN spacing at the center of the crystal versus the total number of particles.

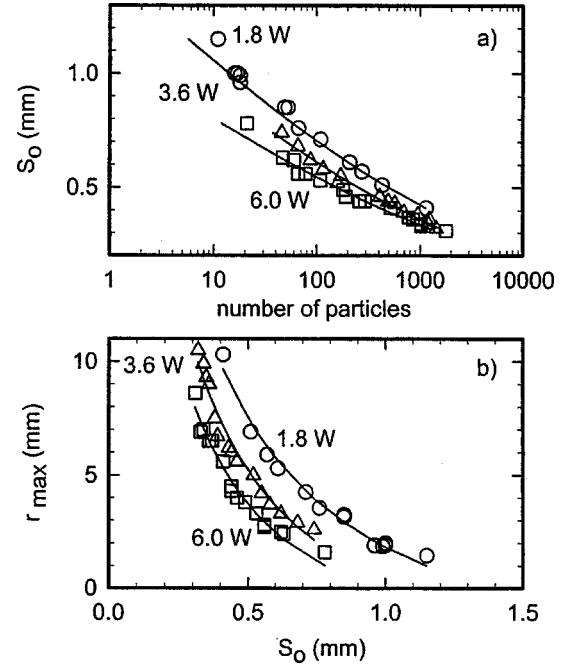


FIG. 5. Nearest-neighbor separation in the plasma crystal center as a function of the number of particles (a), and maximum radial dimension of the plasma crystal as a function of the nearest-neighbor separation in the center of the plasma crystal (b). The rf power was 1.8, 3.6, and 6.0 W at a pressure of 100 mTorr and particle diameter of $8.3 \mu\text{m}$. The solid lines are fits to the data using Eqs. (28) and (26) for plots (a) and (b), respectively.

Using Eqs. (26) and (28), values for N_{tot} , r_{max} , and s_0 derived from crystals of different sizes were fit to directly determine Z and λ . For one set of plasma conditions, the upper plot in Fig. 5 shows s_0 as a function of N_{tot} , while the lower plot in Fig. 5 shows r_{max} as a function of s_0 . Equations (26) and (28) were independently fit to the experimental data to derive values for Z and λ . Those values are discussed below (Fig. 10). In general, the agreement between the two methods is quite good and the uncertainties in the values are approximately $\pm 10\%$. The uncertainties in Z and λ are based upon the uncertainty in the measurements of the values of N_{tot} , r_{max} , and s_0 and the fitting algorithm.

3. Corrections for non-nearest-neighbor interactions

In the full “molecular dynamics” simulations of the dust particle motion and crystallization, we include the pair interaction summed over all dust particles. However, in the EOS analysis, only the NN interactions were included because of the short range of the exponentially shielded nature of the Debye interaction. In the study of finite 2D Yukawa lattices [37] it is desired to have the EOS applicable to highly compressed systems where the interaction of non-NN interactions is important. We can make an approximate correction for non-NN effects by the following.

Consider a single particle in a regular 2D hcp lattice. There are six NN particles at the distance s . The next group has twice as many particles close to the distance $2s$, three times at $3s$, and so on. This total interaction, per pair, is approximately

$$V_{\text{pair}}(s) + 2V_{\text{pair}}(2s) + 3V_{\text{pair}}(3s) + \dots, \quad (29)$$

which for the Yukawa or Debye form of the pair potential is easily summed to give

$$V_{\text{eff}}(s) = V_{\text{pair}}^{\text{Debye}}(s) / [1 - \exp(-s/\lambda)]. \quad (30)$$

Exact lattice summations might be possible for the 2D hcp lattice, but we do not have them at hand.

Equations (20), (21), and (23) may be used as written, replacing V_{pair} with V_{eff} to derive the integrals similar to Eqs. (25) and (28). The relation connecting the radial distance to NN separation s is

$$r^2(s) = 3\alpha \left[\frac{3}{(s/\lambda)} \frac{1}{e^{s/\lambda} - 1} + \frac{e^{s/\lambda}}{(e^{s/\lambda} - 1)^2} \right]_{s_0}^{s_0}. \quad (31)$$

The dimensionless constant α is [37]

$$\alpha = \frac{Z^2 e^2}{4\pi\epsilon_0} \frac{1}{k} \frac{1}{\lambda^3}, \quad (32)$$

where k is the radial restoring force constant as defined in Eq. (13). The relation relating the total number of particles to the NN separation at the center of the dust crystal is

$$\sqrt{3}\alpha \frac{e^{s_0/\lambda}(1 + s_0/\lambda) - 1}{(s_0/\lambda)^3(e^{s_0/\lambda} - 1)^2} = \frac{1}{2\pi} N_{\text{total}}. \quad (33)$$

This shows that the NN separation at the center of the dust crystal is a function of only the ratio N_{total}/α for given plasma conditions as contained in the shielding distance λ . Analogous to Eq. (26), we can evaluate the radius of the crystal at which the NN separation becomes infinite, which is close to the observed radius,

$$r_{\infty}^2 = 3\alpha \left(\frac{3}{(s_0/\lambda)} \frac{1}{e^{s_0/\lambda} - 1} + \frac{e^{s_0/\lambda}}{(e^{s_0/\lambda} - 1)^2} \right). \quad (34)$$

Totsuji, Totsuji, and Tsuruta [37] did molecular dynamics simulations of dust crystals interacting with Debye-shielded (Yukawa) interactions containing several thousand particles. Some of these crystals were in a high relative state of compression where the non-NN interactions are important. The utility and validity of our EOS can be ascertained by comparing the solution to Eqs. (33) and (31) to their simulations. In Fig. 6 we compare with their data for $N_{\text{total}} = 10\,000$ for a wide range of α values. Large α is typical of strong shielding and/or weak confinement (our experimental situation), and small α is typical of strong confinement and/or weak shielding. In order to do this, we solve Eq. (33) numerically for s_0/λ given α and N_{total} , and then evaluate the dependence of $r(s)$ and $s(r)$ from Eq. (31). We find that our non-NN EOS compares quite well with the simulation results except for the very highest compression case in Fig. 6 where the density is 25% low (15% too large in NN separation).

We compare the NN approximation with the non-NN EOS solution in Fig. 7 for a case typical of the conditions in our experiments. The fractional error in NN separation is seen to be 7% (13% in density) for these conditions of

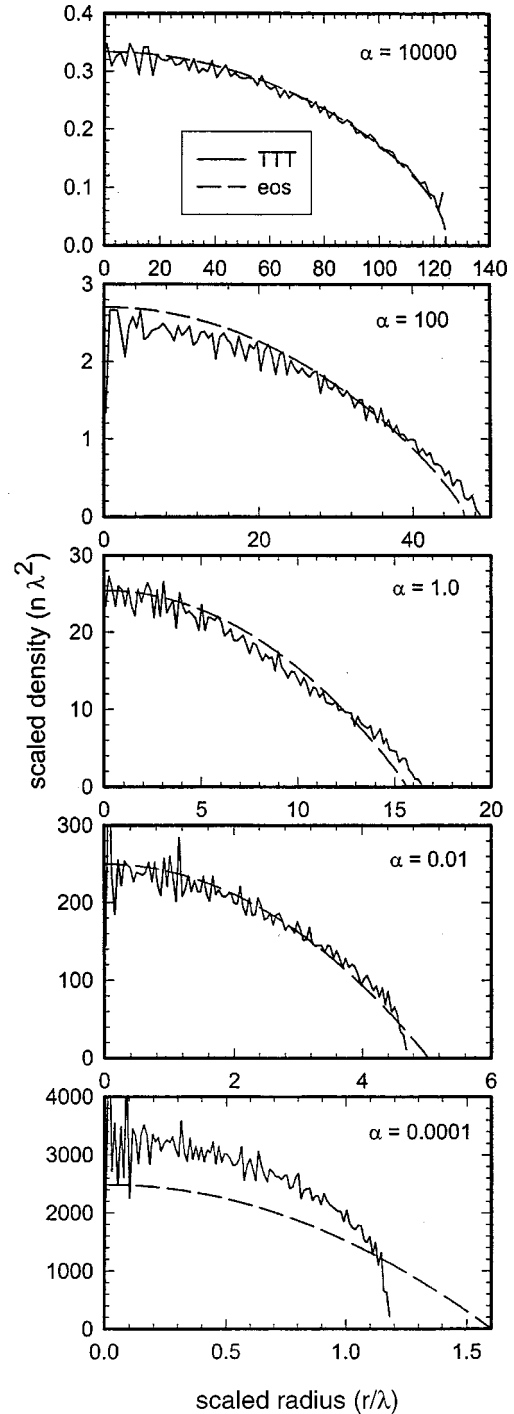


FIG. 6. Comparison of our EOS solution with the simulation data of Totsuji, Totsuji, and Tsuruta (denoted TTT) for various states of compression as denoted by the parameter α . The total number of dust particles is 10 000. The density is multiplied by the Debye length squared, and the radius is divided by the Debye length, to effect the scaling. The agreement is excellent except for the very strongly compressed case $\alpha = 0.0001$, where the s_0/λ ratio is 0.0215.

$N_{\text{total}} = \alpha = 100$. The fractional error implied in the NN approximation is considerably larger for larger N_{total} and α where the ratio s_0/λ falls much below 1. The result of this comparison against the simulations of Totsuji, Totsuji, and

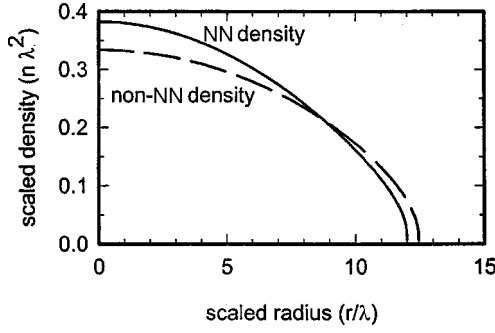


FIG. 7. Comparison of NN EOS with the non-NN approximation for the EOS. The total number of particles N_{tot} is 100 and the dimensionless parameter α is also 100. Scaling is same as Fig. 6.

Tsuruta is that our EOS approximation based on Eqs. (26) and (28), using only nearest neighbors is quite adequate for analyzing the 2D crystal properties, except at high compressions, which we cannot achieve in any case with our experimental arrangement. Moreover, the EOS-type analysis would seem to be adequate for all but the very highest compressions if the EOS were corrected as given in Eqs. (33) and (34) for the non-NN interactions.

IV. SINGLE-PARTICLE TRAJECTORIES IN THE PARABOLIC WELL

For our equation of state analysis to succeed, we must know the pressure due to the curvature of the confining potential well. While the lower electrode shape is parabolic by design, there is no *a priori* assurance that the 2D plasma dust crystal layer or the plasma sheath conforms to the electrode shape. One could argue that for most conditions, the plasma sheath thickness and screening lengths are small compared to the curvature of the electrode, and thus the sheath should be conformal to the electrode curvature. However, for some experimental conditions, notably pressures below 50 mTorr and radius of curvatures of less than 0.3 m, there is evidence that the sheath curvature is no longer parabolic [19]. Thus we must confirm the sheath curvature for a given set of experimental conditions.

Particle trajectories that fall down into the stable layer, necessitate all the details of the dynamics presented in Sec. III. However, once the particles have been trapped in the presheath or sheath layer, their motion is confined to the nearly planar region of the disk that forms from many particles. In this two-dimensional region, a single particle sees only the weak, nearly horizontal, forces due to gravity and the viscous drag due to motion with respect to the background neutral gas. The ion wind force (slightly nonvertical) is perpendicular to the motion and does not accelerate the particle once trapped. The thermophoretic force \vec{f}_{tp} is likewise assumed to be perpendicular to the electrode and the layer of trapped ions. It is to be noted that the analysis of the pairwise interaction does not really depend upon these forces being exactly perpendicular to the horizontal motion in the disk layer. Whatever force is observed to cause the single-particle motion into the confining well will also be operative in the many-particle layer. The only assumption is that the

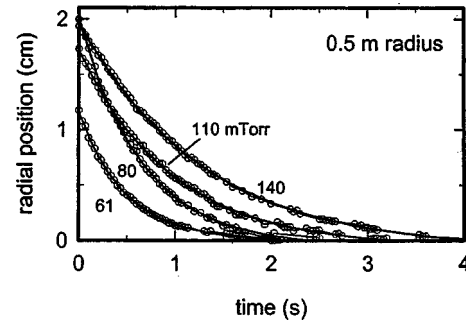


FIG. 8. Radial position of single particles as functions of time for several pressures (mTorr). R_e was 0.5 m and rf power was 1.8 W in argon. Solid lines are single exponential fits.

plasma does not change character with the addition of many particles.

In this two-dimensional sheet we can approximate the Newtonian equation of motion as

$$\begin{aligned} m_d \ddot{\vec{r}} &= -m_d \gamma_{\text{gas}} \dot{\vec{r}} + \hat{e}_r f_r = -m_d \gamma_{\text{gas}} \dot{\vec{r}} - \hat{e}_r m_d g h'(r) \\ &\approx -m_d \gamma_{\text{gas}} \dot{\vec{r}} - \hat{e}_r k r, \end{aligned} \quad (35)$$

where f_r has been given in Eq. (13). If the angular momentum of the particle has damped sufficiently we may replace this 2D equation with the one-dimensional equation in Cartesian coordinate x . This becomes a simple damped oscillator equation, which is harmonic if $h(r)$ is parabolic,

$$\begin{aligned} \ddot{x} &= -\gamma_{\text{gas}} \dot{x} - g h'(x), \\ \ddot{x} &\approx -\gamma_{\text{gas}} \dot{x} - \omega^2 x, \\ \omega^2 &= k/m_d. \end{aligned} \quad (36)$$

The harmonic case can be analyzed by substitution of an exponential, $x = a \exp(-bt)$, showing the usual oscillatory, damped, and intermediate behavior. The simple interesting result is for damped motion in which a plot of the ratio of velocity to position should give the desired constants,

$$-\dot{x}/x = \omega^2/\gamma_{\text{gas}} = (k/m_d)/\gamma_{\text{gas}} = 2cg/\gamma_{\text{gas}} = g/R_e \gamma_{\text{gas}} = b, \quad (37)$$

$$x(t) \propto \exp(-bt).$$

Experimentally, the shape of the well was determined by analyzing trajectories of single particles dropped into the well. Vertical motion shows damped oscillations but the horizontal motion does not show oscillations (overdamped) at our pressures [25]. Particle locations were recorded after their motion had completely damped in the vertical (z) direction (< 1 s) [25]. Examples of time-dependent radial positions for 8.3- μm -diameter particles, for a range of pressures, are shown in Fig. 8. The data is fit to a functional form of $r(t) = r_0 + a \exp(-bt)$ where r_0 is a small radial offset due to measurement inaccuracy. The fits are shown as the solid lines in Fig. 8. For the range of particle diameters and pressures

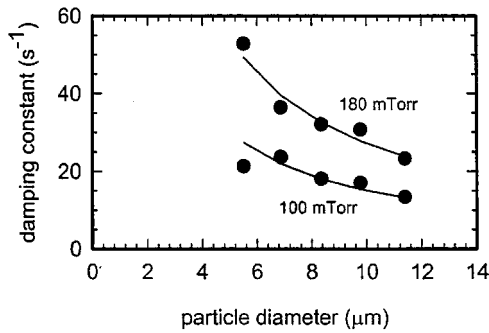


FIG. 9. Damping rate as function of particle diameter for pressures of 100 and 180 mTorr. The rf power was 1.8 W and the R_c was 0.5 m. Solid lines connect calculated decay rates assuming diffusive gas scattering.

investigated in this work, excellent agreement with the single exponential decay was obtained.

Exponential fits were used to determine the damping constant due to gas friction γ_{gas} . Measured damping constants are shown in Fig. 9 as functions of particle diameter and pressure. The solid lines are calculated using gas damping rates evaluated from Eq. (4), assuming diffuse scattering of the neutral gas at 350 K. The 350 K temperature is in good agreement with our laser-induced-fluorescence measurements of the argon metastable temperature at the position of the dust layer and did not strongly depend on gas pressure or power. The agreement of the experimental and predicted decay rates indicates that the plasma sheath conforms to the spherical electrode depression to form a parabolic potential over a wide experimental parameter space. These measurements serve to both verify that the Epstein formulation for particle gas drag applies in this regime and confirm that the shape of the particle trap formed by the plasma sheath is parabolic. The agreement with the exponential fit also indicates that horizontal forces due to thermophoresis or ion wind (drag) are sufficiently small so that they do not contribute to lateral particle acceleration. Additionally, side views of the single-layer 2D plasma crystals showed the crystal curvature was always consistent with R_e .

V. EXPERIMENTAL DETERMINATION OF Z AND λ

The screening length and charge on the particle were determined for a range of rf powers, pressures, and particle diameters. For the case of 8.3- μm -diameter particles, the screening length and charge are shown in Fig. 10 as functions of the rf power and pressure. The two points for each experimental condition correspond to the values determined from independent fits to Eqs. (26) and (28). In most cases, the two values agree to within the uncertainty. The values of Z and λ are in good agreement with rough calculations based upon probe measurements of the electron density and temperature. For example, for the 8.3- μm -diameter particles, the electron temperature is approximately given by T_e (K) $\approx 1.005Z$ since $q \approx 16\pi\epsilon_0 dkT_e/e$, where d is the diameter of the particle. Using a double probe, the measured electron temperatures of 2.6–3.6 eV are in reasonable agreement with temperature predicted by the charge on the particles of

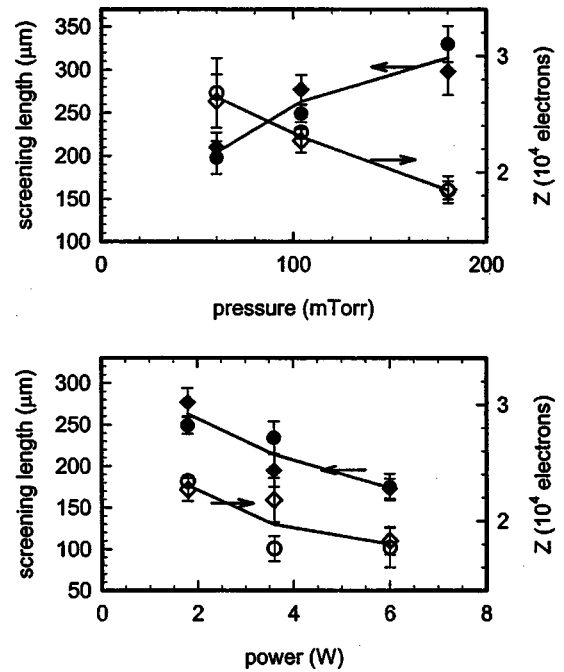


FIG. 10. Screening length and number of electrons on the particles as functions of the pressure (a) and rf power (b). The particle diameter was 8.3 μm . For (a), the power was 1.8 W, and for (b) the pressure was 110 mTorr. The data represented by \bullet were obtained from fits to Eq. (26) as illustrated in Fig. 5(a). The data represented by \blacklozenge were obtained from fits to Eq. (28) as illustrated in Fig. 5(b).

18 000–27 000 K. Similarly, the calculated screening lengths based upon the ion Debye length are on the order of 300 μm . However, the uncertainty in our measurements of Z and λ is improved because we *do not* rely on Langmuir probe measurements or any sheath model for their determination. Our procedure relies solely on the determination of the lateral forces acting on the dust particles and the observed compression of the 2D lattice. Our values for Z and λ are also in reasonable agreement with several previously reported values, to within differences in the plasma conditions and geometry [8,21–25]. For example, Holmann, Melzer, and Piel report values of $Z=8300 \pm 120$, which does not include a 40% uncertainty due to Langmuir probe measurements [24]. Tomme *et al.* reports $Z \sim 30\,000 \pm 10\,000$ using an analysis of the particle oscillation when it is dropped onto the electrode sheath and an analytical model of the shape of the sheath [25].

Screening length and charge on the particles are shown in Fig. 11 as functions of the particle diameter for two chamber pressures. Both the screening length and the charge increase monotonically with increased particle diameter. The increase of Z with diameter is to be expected from the basic charge-potential relation given in Eq. (11), and the connection of the floating potential to electron temperature, $V_f \approx -4kT_e/e$, knowing that the electron temperature should be nearly constant throughout the plasma. However, as we will show below, particles of different mass are located at different heights above the lower electrode and thus at different locations within the plasma sheath. Because the ion energy and electron density are strong functions of position within the

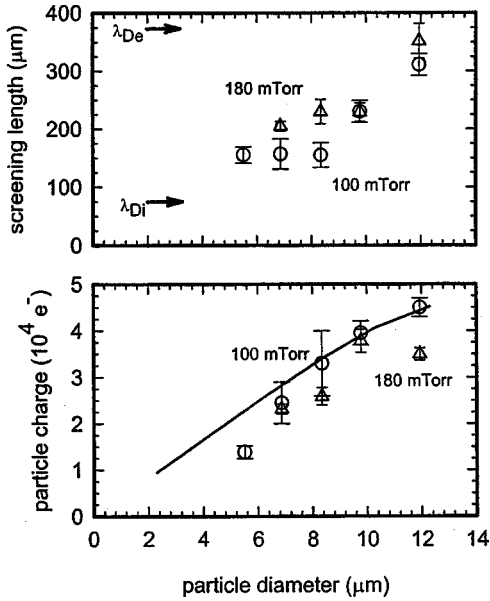


FIG. 11. Screening length and number of electrons on the particles as functions of the particle diameter for pressures of 100 (○) and 180 (△) mTorr. The rf power was 1.8 W. The points connected by a curved line are the results of simulations of charging as discussed in the text. The two lines in the upper plot are the values of the electron and ion screening lengths for appropriate conditions.

sheath, the local plasma conditions that determine λ are not the same for different diameter particles. Therefore, one must account for spatial variations in the plasma when predicting λ as a function of the particle diameter. To examine this more thoroughly, we used the full equations of motion developed in Sec. III A of single dust particles as they were released into a plasma with typical properties. Based upon probe measurements, the bulk density was set at $3 \times 10^8 \text{ cm}^{-3}$ and the electron and ion temperatures in eV were 3.0 and 0.1. The phenomenological parameters characterizing the z dependence of the plasma sheath potential, discussed in Sec. III A 2, were set to give a dc bias on the electrode of -45 V , a match point of quadratic to exponential tail at 3 mm, and a characteristic length of the presheath potential of the electron Debye length. The bulk Debye lengths for the electrons and ions separately were 372 and 74 μm , which is shown in Fig. 11. These two values bound the measured screening lengths of the dust particles. The computed dust charge on the particles is also shown in Fig. 11 and agrees very well with the data.

VI. DETERMINATION OF THE ELECTRIC FIELD

In an rf driven discharge, both the shape and the magnitude of the electric field in the sheath are time dependent. However, the relatively heavy dust particle responds to the time average of the electric field. It is this time-averaged electric field that levitates the plasma dust crystal. The 2D plasma dust crystals form stable single-layer structures at the location where the acceleration due to gravity and, in some cases, ion wind, is balanced by the local electric field as seen from the vertical component of Eq. (1),

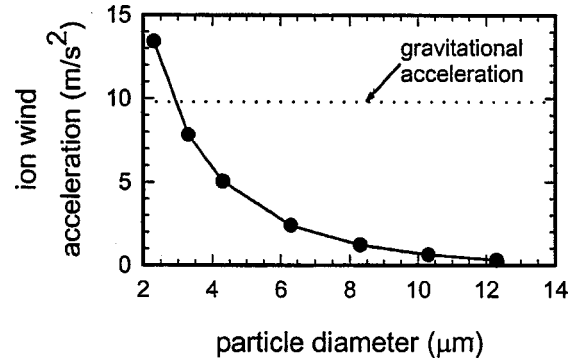


FIG. 12. Calculated acceleration on the particle due to ion wind. The bulk plasma density was $3 \times 10^8 \text{ cm}^{-3}$ and the electron and ion temperatures were 3.0 and 0.1 eV. The lines are drawn to connect the points and to guide the eye.

$$-m_d g + m_d a_w = ZeE_z, \quad (38)$$

where the wind acceleration is written as $a_w = f_w / m_d$. Based upon the ion trajectory data, thermophoretic forces have been neglected. In some cases, the ion wind force complicates a direct calculation of the levitating electric field. Figure 12 shows the ion wind force expressed as acceleration in order to compare with the acceleration due to gravity. As with the calculations of Z just discussed, the bulk density was set to $3 \times 10^8 \text{ cm}^{-3}$ and the electron and ion temperatures were 3.0 and 0.1 eV. For particles with diameter greater than $\approx 6 \mu\text{m}$, the ion wind force is less than 25% of the force of gravity and may be neglected. However, for higher electron densities or smaller particle diameters, the ion wind force becomes more important. For example, a density of $1 \times 10^9 \text{ cm}^{-3}$ and electron temperature of 2.5 eV results in an ion wind acceleration of $\approx 7 \text{ m/s}^2$ for a 6- μm -diameter particle. Thus ion wind is not always a negligible component of the vertical force balance. Unfortunately, it is difficult to accurately account for the ion wind force when it is comparable to the gravity because the calculation depends on probe measurements of the electron density and temperature, which can have significant uncertainty. However, for the largest particles used in this work, 8–12 μm , and to within the uncertainty of our probe measurements, the influence of ion wind is small compared with gravity. In this case we can use the measurements of dust charge to obtain the plasma presheath electric field *without any assumptions* about the plasma properties.

Assuming that the ion wind force is negligible, the levitating electric field as a function of height can be directly calculated from the measured Z (Fig. 11). The derived, time-averaged electric field is shown in Fig. 13 for two pressures. For these conditions, the electric field varies between 5 and 22 V/cm. The solid lines are single exponential fits with a scale length of $1.2 \pm 0.15 \text{ mm}$. For the larger particles (the three leftmost points for each pressure) the acceleration due to ion wind is significantly smaller than gravity and as such can be neglected. However, for the smaller diameter particles, the actual electric field is larger than the plotted values due to the ion wind force. Depending on the exact density

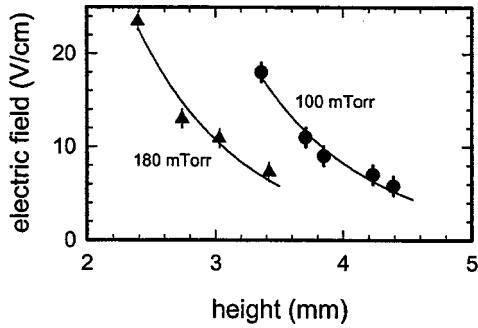


FIG. 13. Time-average electric field as a function of height above the lower electrode for pressures of 100 and 180 mTorr. These values neglect particle acceleration due to the ion wind. The rf power was 1.8 W. The solid line is a single exponential fit with a scale length of 1.2 ± 0.15 mm.

and temperature, the electric field could be up to 30%–50% larger.

The electric field measurements can be indirectly verified by measurements of the spatial derivative of electric field. Holmann and coworkers showed that the application of a small amplitude modulation (AM) (5%) to the rf driven voltage can produce a resonance in the vertical motion of the particles [24]. At low AM frequencies (a few hertz), the particles will respond to the plasma sheath oscillations. For our conditions, at AM frequencies on the order of 20 Hz, the particle vertical motion goes through a maximum before decaying to zero at higher frequencies. Briefly, the motion of the particle trapped at the sheath edge can be described by the solution of a harmonic oscillator. The spatial derivative of the electric field can be expressed as $\partial E/\partial x = \omega_0^2 m_{\text{dust}}/Ze$, where ω_0 is the resonant frequency. We measured the resonant frequency for a range of particle diameters by observing the particle motion from the side of the chamber as the AM frequency was varied. The spatial derivatives are shown in Fig. 14. The displayed error bars are due to the uncertainty in the peak of the resonant frequency and the charge on the particle. The solid lines are the spatial derivative of the exponential fits shown in Fig. 13. The good agreement between the measured derivatives and the calculated derivatives based upon the data in Fig. 12 is encouraging and

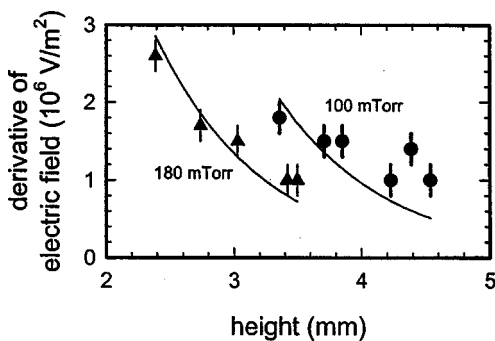


FIG. 14. Spatial derivative of the time-average electric field as a function of height above the electrode for pressures of 100 and 180 mTorr. The rf power was 1.8 W. The solid line is the spatial derivative of the exponential fit shown in Fig. 13.

not unreasonable considering the uncertainty in the measured electron density and temperature. However, the calculations of the ion wind discussed above prohibit a complete neglect of the ion wind force and will require further investigation.

Several points can be observed from the magnitude of the electric field and shape of the distribution with dust particle mass. Due to the difficulties in conducting experiments in this region and challenges associated with predictive simulation of this region of the discharge, relatively little activity has been directed to this region of the discharge. In this work, the rf driven frequency is significantly above the ion plasma frequency for the argon ions. As a result, the ions will respond only to the time-averaged electric field. For an electric field of 20 V/cm and a pressure of 100 mTorr, the argon ion drift energy is ≈ 0.3 eV (as determined from drift velocity as a function of E/p) [38], well below the measured electron temperature of 3.1 eV. Thus the 2D plasma dust crystal forms on the bulk plasma side of the classical sheath Bohm point.

Second, Tomme and co-workers suggested that the vertical oscillation frequency of a particle dropping onto the plasma sheath could be used to derive the charge on the particle [25]. They extrapolated measured electric field distributions close to the sheath surface to the region where the plasma crystals form and used a linearly varying electric field as the potential energy term to fit the oscillation frequency. While the framework of the analysis is valid, this data would indicate that the form of the electric field that was used in those fits may not have been correct and that the resulting values of particle charge may not be accurate. Unfortunately, the ill-defined (except for theory) nature of the ion wind for a fraction of our parameter space makes a definitive statement of the plasma sheath structure difficult.

Finally, we find that the shape of the electric field in this region is not linear, as is observed in the higher electric field regions of the sheath closer to the electrode surface [1–3]. In addition, the sheath width is smaller for the higher pressure, as expected. These observations are consistent with the measurements of Oksuz and co-workers that showed a nonlinear ion velocity distribution at the sheath bulk transition [4]. Comparison of our measured spatial distribution and the predicted shape given by Riemann shows some points of agreement [5]. For a weakly collisional plasma similar to our conditions, Reimann predicted a functional form for the presheath potential of

$$\Phi = \frac{T_e}{e} \sqrt{\frac{x}{\lambda_{\text{Debye}}}}. \quad (39)$$

Using this functional form, the fits to our data were not as good as a single exponential. However, this functional form would indicate that the electric field is higher than an exponential at a larger distance from the electrode surface, in agreement with the influence of the ion wind. Thus additional work needs to be done to understand the shape of the potential distribution in the presheath.

VII. SUMMARY

Particle interactions were directly determined from the lateral compression of two-dimensional plasma dust crystals confined in a parabolic potential well. Unlike prior techniques used to derive the number of electrons on the particles Z and the screening length λ , this method does not rely on measurements of the plasma parameters, thus reducing a major source of uncertainty. The shape of the parabolic potential well was confirmed by observing trajectories of single particles falling within the well. Particle trajectories are in good agreement with values calculated using gas temperatures derived from laser-induced-fluorescence measurements of the argon metastable velocity distributions and assuming diffusive gas scattering.

Measured particle separations combined with an equation of state for the crystal were used to derive values for the particle screening length and the charge on the particles. Particle screening length and charge were measured for a range of plasma power, pressure, and particle diameter (mass). Plasma crystal compression in the parabolic potential was demonstrated to be in good agreement with that predicted by an equation of state for the 2D dust layer incorporating De-

bye shielding of the charges. Analysis of the particle heights and charge were used to derive the time-average electric field at edge of the rf driven plasma sheath. These measurements show that the particles are confined to the on the bulk plasma side of the classical Bohm point and that the sheath has a nonlinear spatial dependence. Measurements of the spatial derivative of the time-average electric field support the measurement of a nonlinear variation of the electric field as a function of height above the electrode in the presheath region. We note that the ion wind force can significantly influence the vertical location of the particles according to our simulations, and that the impact of that force is currently difficult to quantify.

ACKNOWLEDGMENTS

The authors thank Paul Miller for the double probe measurements and Professor H. Totsuji for sharing the data in Fig. 6. This work was performed at Sandia National Laboratories and was supported by the Division of Material Sciences, Basic Energy Sciences, U.S. Department of Energy and Sandia National Laboratories (Grant No. DE-AC04-94AL85000).

-
- [1] V. P. Pavlenko, H. J. Kim, T. Ikutake, J. B. Kim, Y. W. Choi, M. D. Bowden, and K. Muraoka, *Phys. Rev. E* **62**, 7201 (2000).
 - [2] U. Czarnetzki, D. Luggenholcher, and H. F. Dobele, *Appl. Phys. A: Mater. Sci. Process.* **A72**, 509 (2001).
 - [3] G. A. Hebner, K. E. Greenberg, and M. E. Riley, *J. Appl. Phys.* **76**, 4036 (1994).
 - [4] L. Oksuz, M. Atta Khedr, and N. Hershkowitz, *Phys. Plasmas* **8**, 1729 (2001).
 - [5] K.-U. Riemann, *Phys. Plasmas* **4**, 4158 (1997).
 - [6] J. H. Chu and I. Lin, *Phys. Rev. Lett.* **72**, 4009 (1994).
 - [7] H. Thomas *et al.*, *Phys. Rev. Lett.* **73**, 652 (1994).
 - [8] U. Konopka, G. E. Morfill, and L. Ratke, *Phys. Rev. Lett.* **84**, 891 (2000).
 - [9] P. K. Shukla, *Phys. Plasmas* **8**, 1791 (2001).
 - [10] D. H. E. Dubin, *Phys. Rev. Lett.* **71**, 2753 (1993).
 - [11] V. M. Bedanov and F. M. Peeters, *Phys. Rev. B* **49**, 2667 (1994).
 - [12] H. Totsuji, T. Kishimoto, and C. Totsuji, *Phys. Rev. Lett.* **78**, 3113 (1997).
 - [13] L. Candido *et al.*, *J. Phys.: Condens. Matter* **10**, 11 627 (1998).
 - [14] H. Totsuji, *Phys. Plasmas* **8**, 1856 (2001).
 - [15] X. P. Huang *et al.*, *Phys. Rev. Lett.* **80**, 73 (1998).
 - [16] J. J. Bollinger *et al.*, *Phys. Plasmas* **7**, 7 (2000), and references therein.
 - [17] E. R. Dufresne *et al.*, *Phys. Rev. Lett.* **85**, 3317 (2000).
 - [18] T. M. Squires and M. P. Brenner, *Phys. Rev. Lett.* **85**, 4976 (2000).
 - [19] G. A. Hebner, M. E. Riley, D. S. Johnson, Pauline Ho, and R. J. Buss, *Phys. Rev. Lett.* **87**, 235001 (2001).
 - [20] M. Lampe *et al.*, *Phys. Rev. Lett.* **86**, 5278 (2001).
 - [21] D. A. Law *et al.*, *Phys. Rev. Lett.* **80**, 4189 (1998).
 - [22] S. Samsonov *et al.*, *Phys. Rev. Lett.* **83**, 3649 (1999).
 - [23] A. Holmann *et al.*, *Phys. Rev. E* **56**, 7138 (1997).
 - [24] A. Holmann, A. Melzer, and A. Piel, *Phys. Rev. E* **59**, R3835 (1999).
 - [25] E. B. Tomme *et al.*, *Phys. Rev. Lett.* **85**, 2518 (2000).
 - [26] M. Klindworth *et al.*, *Phys. Rev. B* **61**, 8404 (2000).
 - [27] W.-T. Juan *et al.*, *Phys. Rev. E* **58**, R6947 (1998).
 - [28] V. Steinberg *et al.*, *Phys. Rev. Lett.* **86**, 4540 (2001).
 - [29] P. J. Hargis Jr. *et al.*, *Rev. Sci. Instrum.* **65**, 140 (1994).
 - [30] J. C. Crocker and D. G. Grier, *J. Colloid Interface Sci.* **179**, 298 (1996).
 - [31] P. S. Epstein, *Phys. Rev.* **23**, 710 (1924).
 - [32] M. A. Gallis, J. Torczynski, and D. J. Rader, *Phys. Fluids* **13**, 3482 (2001).
 - [33] M. A. Gallis, D. J. Rader, and J. Torczynski, *Aerosol Sci. Technol.* (to be published).
 - [34] M. D. Kilgore, J. E. Daugherty, R. K. Porteous, and D. B. Graves, *J. Appl. Phys.* **73**, 7195 (1993).
 - [35] J. E. Allen, *Phys. Scr.* **45**, 497 (1992); with first usage in H. M. Mott-Smith and I. Langmuir, *Phys. Rev.* **28**, 727 (1926).
 - [36] F. Melandsø, T. Nitter, T. Aslaksen, and O. Havnes, *J. Vac. Sci. Technol. A* **14**, 619 (1996).
 - [37] H. Totsuji, C. Totsuji, and K. Tsuruta, *Phys. Rev. E* **64**, 066402 (2001).
 - [38] J. A. Hornbeck, *Phys. Rev.* **84**, 615 (1951).